Journal of Energy Chemistry 71 (2022) 604–611

Contents lists available at ScienceDirect

Journal of Energy Chemistry

journal homepage: www.elsevier.com/locate/jechem

http://www.journals.elsevier.com/journal-of-energy-chemistry/

Enhanced efficiency and stability in Sn-based perovskite solar cells by trimethylsilyl halide surface passivation

Zheng Zhang [a,*], Liang Wang [a], Ajay Kumar Baranwal [a], Shahrir Razey Sahamir [a], Gaurav Kapil [a], Yoshitaka Sanehira [a], Muhammad Akmal Kamarudin [a], Kohei Nishimura [a], Chao Ding [a], Dong Liu [a], Yusheng Li [a], Hua Li [a], Mengmeng Chen [a,*], Qing Shen [a,*], Teresa S. Ripolles [b], Juan Bisquert [c], Shuzi Hayase [a,*]

[a] Graduate School of Informatics and Engineering, University of Electro-Communication, 1-5-1 Chofugaoka, Chofu, Tokyo 182-8585, Japan
[b] Escuela Técnica Superior de Ingeniería de Telecomunicación, Universidad Rey Juan Carlos, Madrid 28933, Spain
[c] Institute of Advanced Materials (INAM), Universitat Jaume I, Castelló 12006, Spain

ARTICLE INFO

Article history:
Received 23 December 2021
Revised 24 February 2022
Accepted 18 March 2022
Available online 26 March 2022

Keywords:
Tin halide perovskite
Trimethylsilyl halide
Surface passivation
Stability

ABSTRACT

Lead free tin perovskite solar cells (PKSCs) are the most suitable alternative candidate for conventional lead perovskite solar cells. However, the efficiency and the stability are insufficient, mainly because of the poor film quality and numerous defects. Here we introduce an efficient strategy based on a simple trimethylsilyl halide surface passivation to increase the film quality and reduce the defect density. At the same time, a hydrophobic protective layer on the perovskite surface is formed, which enhanced the PKSCs' stability. The efficiency of the solar cell after the passivation was enhanced from 10.05 % to 12.22% with the improved open-circuit voltage from 0.57 V to 0.70 V. In addition, after 92 days of storage in N_2 filled glovebox, the modified T-PKSCs demonstrated high stability maintaining 80% of its initial efficiency. This work provides a simple and widely used strategy to optimize the surface/interface optoelectronic properties of perovskites for giving more efficient and stable solar cells and other optoelectronic devices.

1. Introduction

Since Kojima's first synthesized organic–inorganic hybrid lead-halide perovskite solar cells (PKSCs) in 2009 [1], organic–inorganic halide perovskite solar cells (PSCs) have drawn tremendous attention because their power conversion efficiencies (PCE) have soared to 25.5% [2]. However, since these halide perovskite materials contain the toxic lead ion (Pb^{2+}) [3,4], many companies hesitate to put them into practical uses.

Therefore, several elements have been proposed, including Sn [5], Ge [6], Cu [7], Bi [8], and Sb [9]. Among all these alternatives, Sn ion is the most suitable one for replacing the Pb ion, because of the same valence and the similar ionic radius (Sn^{2+} 1.35 Å and Pb^{2+} 1.49 Å) [10,11]. Tin perovskite solar cells with over 14% efficiency [12,13] have been reported. However, the power conversion efficiency and the stability of Sn perovskite solar cells were insufficient. This is mainly ascribed to defects, such as native point defects, 3D defects and other defects, the kinds of defects all listed into Table S1 [14,15]. If these defects are in the band gap (deep traps), nonradiative recombination of these photo-generated carriers occurs at these defects. These ion vacancies cause the migration of other cations or anions, which facilitate the irreversible chemical decomposition of the perovskite [16,17].

To suppress the formation of defects, several strategies have been reported. For instance, a controlled excess of lead iodide (PbI_2) in the Pb perovskite layer formed a shell around the individual perovskite crystals in the films, and decreases the vacancies accompanied with the improved device performance [18]. Another method is to use additives to suppress the formation of iodide vacancies and multi-vacancies via the formation of hydrogen bonds [19,20], ionic bonds [21] or lattice strain relaxation [22–25].

However, since these additives may trigger uncontrollable nucleation sites [26], the halide vacancies are readily formed at the surface of the polycrystalline perovskite films. Several researches also make a second coating of excess halide ions on the perovskite film surface. Wu et al have used CdI_2 to reduce the surface halide vacancy. Jin et al have coated the MACl solution to lead the secondary growth of the perovskite layer [26,27]. Yang et al have used a facile post treatment of MABr solution which

* Corresponding authors.
E-mail addresses: c2043009@edu.cc.uec.ac.jp (Z. Zhang), chenmengmeng1017@gmail.com (M. Chen), shen@pc.uec.ac.jp (Q. Shen), hayase@uec.ac.jp (S. Hayase).

https://doi.org/10.1016/j.jechem.2022.03.028

converts $MAPbI_3$ to $MAPbI_{3-X}Br_X$ with high quality [28]. As for Sn based perovskite, Joker et al. have introduced Ga^+ into $FASnI_3$ to suppress the formation of iodide vacancies and passivate grain boundaries [29]. Wang et al. have used Phenylhydrazine chloride (PHCl) to passivate the trap states of perovskite film for an enhanced V_{oc} of 0.94 V [30]. Efact et al. also introduced the phenylhydrazinium thiocyanate (PHSCN) with new procedure and solvent to passivate the perovskite surface [31]. What we learnt from the previous reports is that these additives have ionic characters.

Inspired by the above studies, we investigate the passivation of Tin-based perovskite using a new type of the reagent, trimethylsilyl halide (Me_3SiX) having ionic characters of Me_3Si^+ and X^- with the hydrophobicity of the Me_3Si moiety. As far as we know, there are no reports on trimethylsilyl halide passivation on Tin based PKSCs. In this work, the photovoltaic performance affected by trimethylsilyl halide passivation is discussed.

2. Experimental

2.1. Materials

Tin(II) iodide (SnI_2, 99.99%, Sigma-Aldrich), tin(II) fluoride (SnF_2, 99%, Sigma-Aldrich), germanium (II) iodide (GeI_2, >99.8%, Sigma Aldrich), formamidinium iodide (FAI, >98.0%, TCI), ethylenediammonium diiodide ($EDAI_2$, ≥98.0%, Sigma Aldrich), bromotrimethylsilane (Me_3SiBr, ≥97%, TCI), chlorotrimethylsilane (Me_3SiCl, >98%, TCI), iodotrimethylsilane (Me_3SiI, ≥97%, TCI), poly (3,4-ethylenedioxythiophene) polystyrenesulfonate (PEDOT PSS, CLEVIOS PVP AI 4083), N,N-dimethylformamide (DMF, 99.8%, Sigma-Aldrich), dimethyl sulfoxide (DMSO, ≥99.9%, Sigma-Aldrich), chlorobenzene (CB, 99.8%, Sigma-Aldrich) were used without further purification.

2.2. Device fabrication

Firstly, the FTO glasses were cleaned with distilled water, acetone, and isopropanol sequentially for 15 min in each solvent. The substrate was further cleaned with ozone plasma treatment for 5 min. PEDOT:PSS solution passed through a 0.45 μm PVDF filter was spin-coated on the FTO substrate at 5000 r/min for 50 s and then the substrate was annealed at 180 °C for 20 min. All the coated substrates were transferred to a nitrogen-filled glovebox. The 0.98 M FAI, 0.01 M ethylene diammonium iodide ($EDAI_2$), 0.1 M SnF_2 and 0.05 M GeI_2 were stirred in the mixed solvent DMF: DMSO (4:1 v/v) for 4–5 h at ambient temperature [32]. The composition of the perovskite was abbreviated as $FA_{0.98}EDA_{0.01}SnI_3$. The preparation process of perovskite layer and the surface treatment process were showed in Fig. S1. 50 μL of the perovskite precursor solution was spin-coated on the PEDOT: PSS coated substrate at 5000 r/min for 50 s. A 500 μL chlorobenzene as antisolvent was quickly drop-casted at 14–16 s. The $FA_{0.98}EDA_{0.01}SnI_3$ crystallization was completed by annealing the sample at 70 °C for 20 min. Me_3SiBr, Me_3SiCl and Me_3SiI were dissolved in the chlorobenzene to prepare 0.15 mM solution. At the 5 s of the spinning process, the samples were drop-cased with the Me_3SiBr, Me_3SiCl, and Me_3SiI solution, respectively, at 5000 r/min for 50 s. The films were post-annealed at the 70 ℃ for 10 min. The 30 nm of Fullerene (C60), 7 nm of 2,9-dimethyl-4,7-diphenyl-1,10-phenanthroline (BCP), and 120 nm of Ag was prepared consecutively by thermal deposition to fabricate solar cell.

2.3. Photovoltaic measurement

The solar cell measurements were performed by a solar simulator (CEP-2000SRR, Bunkoukeiki Inc, AM 1.5G, 100 mW cm^{-2}) in the air. The measured area was fixed to be 0.1 cm^2 using a non-reflective black metal mask. The scanning rate was 0.1 V/s. The EQE spectra were recorded using a monochromatic Xenon lamp (Bunkouki CEP-2000SRR). The EQE measurement was performed under monochromatic light from 1200 nm to 300 nm. (300 W Xenon lamp with a monochromator, Newport 74010). The electrochemical impedance spectroscopy (EIS) was analyzed with PAIOS software.

2.4. Characterization

The perovskites coated on the glass substrate were used for the following measurements. The X-Ray Diffraction (XRD), Ultraviolet and visible spectrophotometry (UV–Vis), photoelectron yield spectroscopy (PYS), and X-ray photoelectron spectroscopy (XPS), Steady-state photoluminescence (PL), time-resolved PL and water contact angle. The XRD patterns were obtained by a Rigaku Smartlab X-ray diffractometer with monochromatic Cu-Kβ irradiation (45 kV/200 mA). The UV–Vis measurements were performed using a JASCO V-670 Spectrophotometer. PYS was measured using Bunkoukeiki KV 205-HK ionization energy system with the photon energy from 4.5 eV to 6.7 eV and density of state (DOS) were also determined from the PYS spectra. XPS measurement was performed using Shimadzu Kratos Axis-Nova spectrometer. Al *Kα* excitation source was used at pass energy of 80 eV and the energy resolution was 1000 meV. The perovskite layer coated on PEDOT: PSS/ glass substrate was used to measure the surface morphology using FE-SEM (HITACHI S4800) instrument and Bruker Innova atomic force microscopy (AFM) (JSPM5200). A gold electrode (1 cm × 1 cm having 2 μm cross slit) with Van der Pauw geometry was deposited on a glass. The Tin halide perovskite solution was coated on the substrate. for Hall measurement was carried out in a glove box filled with N_2 using ECOPIA Hall effect measurement system (HMS-3000 VER 3.52). The applied current was 1 μA (within the liner curve region).

3. Results and discussion

3.1. Photovoltaic device architecture and performance

For simplification, the solar cell (SC) with the $FA_{0.98}EDA_{0.01}SnI_3$ perovskite without surface passivation is abbreviated as W/T-SC and the solar cell passivated with Me_3SiBr, Me_3SiCl and Me_3SiI is labeled as Me_3SiBr SC, Me_3SiCl SC and Me_3SiI SC, respectively. The device structure in this study is shown in Fig. 1(a). The passivation was performed soon after the perovskite layer was deposited. The current density–voltage (*J-V*) curves of champion PKSCs are shown in Fig. 1b, accompanied with the corresponding photovoltaic parameter in Table 1. After the surface passivation, the PCE increased from 10.05% (W/T SC) to 11.68% (Me_3SiCl SC), 12.22% (Me_3SiBr SC) and 11.58% (Me_3SiI SC). To further confirm the reproducibility of the photovoltaic behaviors, we fabricated 5 devices for each condition and measured their photovoltaic performances. The box chart (Fig. S2) shows the photovoltaic parameters of the Me_3SiX SC. Fig. 1(c) and Table 1 showed the highest photovoltaic properties of Me_3SiBr SC with the efficiency of 12.22%, V_{oc} of 0.70 V, J_{sc} of 24.11 mA cm^{-2}, FF of 0.72, compared with the controlled one (PCE of 10.05%, V_{oc} of 0.57 V, J_{sc} of 24.62 mA cm^{-2}, FF of 0.71). The enhanced PCE is mainly due to the higher V_{oc} and FF. The J_{sc} decrease may be due to a little reduced thickness of the perovskite layer caused by the etching effect with the chlorobenzene (CB) used as the solvent of Me_3SiBr (Fig. S3). To further certificate, we also made the PKSCs with the CB prostrated perovskite film, and observed the decrease in J_{sc} (Fig. S4). The J_{sc} calculated from EQE (Fig. 1d) was almost the same as the J_{sc} measured.

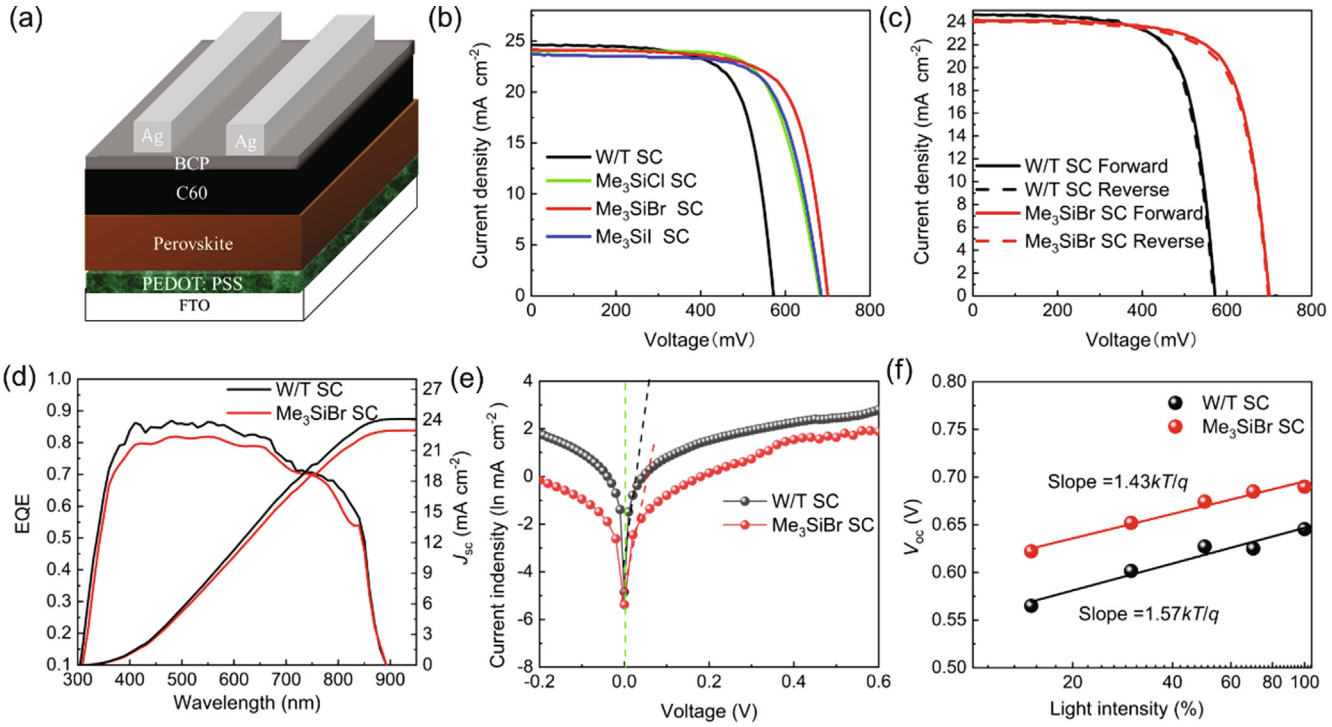

Fig. 1. (a) Device architecture of invert perovskite planar heterojunction solar cell, (b) and (c) *J-V* characteristics for champion PKSCs without/with surface passivation under 1.5 G simulated sunlight illumination (100 mW cm^{-2}). (d) External quantum efficiency (EQE) spectra, (e) dark *J–V* curves, (f) light intensity dependence of open-circuit voltage (V_{oc}).

Table 1
Photovoltaic parameter of champion PKSCs after each passivation.

Sample	Scan direction	J_{sc} [mA cm^{-2}]	V_{oc} [V]	FF	PCE [%]
W/T-SC	Forward	24.62	0.57	0.71	10.05
	Reverse	24.65	0.57	0.71	9.95
Me_3SiCl-SC	Forward	24.01	0.68	0.71	11.68
	Reverse	23.86	0.69	0.66	10.83
Me_3SiBr-SC	Forward	24.11	0.70	0.72	12.22
	Reverse	24.05	0.69	0.71	11.95
Me_3SiI-SC	Forward	23.69	0.68	0.71	11.58
	Reverse	23.71	0.69	0.67	10.94

The dark current and light intensity dependence of open-circuit voltage (V_{oc}) of the devices are shown in Fig. 1(e and f). The dark current density of the $MeSiBr_3$ SC was clearly lower that of W/T-SC, which is usually linked to the carrier recombination loss in the dark [33]. The J_0 obtained from the intercept at 0 V for W/T SC was 7.87 × 10^{-3} mA cm^{-2} while the J_0 for Me_3SiBr SC was 4.61 × 10^{-3} mA cm^{-2}. The lower J_0 shows that the leakage current is low and the carrier recombination was suppressed by the Me_3-SiBr passivation [34,35]. In addition, the recombination process was further analyzed by the light-intensity dependence of J_{sc} and V_{oc} (Fig. 1f), using the following equation.

$$V_{oc} = \frac{nkT}{q} \ln\frac{J_{sc}}{J_0}$$

where n represented the ideality factor, k the Boltzmann constant, T the absolute temperature, q the elementary charge and J_0 the saturation current density (in dark), respectively. Under the condition of $J_{sc} \gg J_0$ and $J_{sc} \propto$ light intensity (L), the equation is described as follows [36].

$$V_{oc} = \frac{nkT}{q} \ln L$$

The ideality factor n obtained from the linear fitting of the plot (light intensity (L) *vs* V_{oc}) decreased from 1.57 (W/T SC) to 1.42 (Me_3SiBr SC). These results imply that Me_3SiBr passivation reduced trap-assisted charge recombination in the devices. The V_{oc} enhancement after the passivation also supports this explanation [37].

To further investigate the charge transfer mechanism on the interfaces, we performed the electrical impedance (EI) measurements for the W/T SC and Me_3SiBr SC under different bias voltages under dark condition. The results are shown in Fig. S5(a and b). These plots were fitted using a simple equivalent circuit of the series resistance (R_s) and the recombination resistance (R_{rec}) [38]. The results are showed in Fig. S5(c and d). The recombination resistance (R_{rec}) was increased after Me_3SiBr surface passivation, implying the reductions in the trap assisted charge recombination and the higher V_{oc} [39]. In addition, the carrier lifetimes (τ_e) were calculated from the formula of $\tau_e = R_{rec} \times C_\mu$ [40]. The longer carrier

life time (τ_e) of Me_3SiBr SC, compared with that of W/T-SC also support the above explanation of the suppressed carrier recombination [41].

The steady photovoltaic performance of Me_3SiBr SC and W/T SC were measured by maximum power point tracking system (MPPT) under 100 mW/cm^2 AM 1.5 G illumination (Fig. 2a). Me_3SiBr SC showed PCE and photocurrent density (J_{sc}) of 10.8% and 20.4 mA cm^{-2}, keeping constant values for 600 seconds. The photovoltaic performance of un-encapsulated devices stored in the N_2 atmosphere were measured every 3 days. The 80% of the efficiency of Me_3SiBr SC was maintained after 92 days storage while the W/T SC's efficiency was dropped to 73% after 37 days. The PCE of the devices exhibited fluctuation during the stability measurement, which may be due to charge accumulation. This phenomenon is not unique for this work but has also been observed previously research, attributed to the lattice strain relaxation of the perovskite crystal [24,42,43].

3.2. Mechanistic study of passivation effect of Me_3SiX

The most plausible working mechanism for the Me_3SiX surface passivation is the reduction of the surface halide deficiency as shown in Fig. 3. It has been reported that the bonding of Me_3Si-X has highly polarized character such as $Me_3Si(\delta^+)X(\delta^-)$ (X is halide) [44,45]. The $Me_3Si^+\bullet X^-$ behaves in the similar way to R-$NH^{3+}\bullet I^-$. The Me_3Si-X supplies X ion to fill the surface iodide vacancies. The Me_3Si^+ remain at the surface as the counter cation of halide.

To reveal the Me_3SiX surface passivation mechanism mentioned above, the top-view SEM/AFM images and water contact angles were measured as shown in Fig. 4. Du. et al have reported that the Pb–Sn perovskite surface passivated with Me_4NBr gives many small flake features attached on the surface [46] and these flakes are formed by halide ion exchange between Br^- and I^-. The same phenomena were observed after the Me_3SiX passivation in our experiments. In addition, the small pinholes disappeared from the surface after the Me_3SiX passivation. The lower pinhole density lessens the leakage current and improved the fill factor of device [47], which was in accordance with the photovoltaic parameters listed in the Table 1. To make it clearer, we also supplied the large-scale SEM images of the surface and the cross section (Fig. S6). In the SEM cross-sectional image (Fig. S6e), the columnar crystal and longitudinal stacking of the perovskite layer were seen with the thickness around 250 nm. The Me_3Si^+ layer was not detected due to the thin thickness because the concentration of the passivation solution was low (0.15 mM). The minimum root mean-square (RMS) roughness was improved from 28.13 nm (W/T) to 21.90 nm (Me_3SiBr) on the basis of the AFM images. A smooth surface gives better contact at ETL (electron transport layer) /perovskite hetero interface, and improves FF [46]. Fig. 4(g and h) showed the contact angle measurements of water on W/T and Me_3SiBr. Larger contact angle was observed for the perovskite films with Me_3SiBr surface passivation, which may be attributed to the hydrophobic properties of the Me_3Si groups remaining of the surface. The Me_3Si moiety will effectively slow down the invasion of water molecules and improve the stability [48].

As shown in Fig. 5(a), $FA_{0.98}EDA_{0.01}SnI_3$ with/without the surface passivation shows the typical XRD peaks corresponding to (100), (120), (200), (211), (222) and (300) facets, which can be ascribed to the (orthorhombic phase). The XRD patterns were normalized using the main peak (100) to further interpret the role of the passivation in the crystal formation. The lattice strain μ can be calculated from Williamson-Hall equation as shown in the Fig. S7.

$$\beta_{\text{total}} \cos\theta = \frac{K\lambda}{D_{\text{size}}} + \mu 4 \sin\theta$$

where β_{total} is the full width half maximum, θ is the Bragg angle, K is the shape factor, λ is the wavelength of the incident X-ray, and D_{size} is the average crystallite size obtained from Scherrer's equation [49]. As shown in the Fig. S7, the lattice strain or disordering (μ) decreased from 0.00873 (W/T) to 0.00533 (Me_3SiBr) after the surface passivation, which may be due to the gradient chemical composition from these grain boundary [50]. The less lattice strain (disordering) results in less non-radiative recombination after surface passivation [35,51]. It was interesting to observed that there was no obviously peak shift (Fig. 5b), implying that the Me_3Si ion is not inserted into the crystal lattice, but remains on the surface.

From the reflective FTIR spectra, as shown in the Fig. 5(c) and Fig. S8, the perovskite films passivated with/without Me_3SiX solution and pure Me_3SiX solution showed nearly the same characteristic peaks around 3250 to 3500 nm and 1500 to 1750 nm. The direct evidence of the presence of the $Me3Si^+$ group on the surface was not obtained. But from the solid-water contact angle result, the surface became hydrophobic after the passivation, implying that Me_3Si group is present at the surface, because it is well-known that Me_3Si group gives hydrophobic properties.

The absorption onset in the UV–Vis spectra was slightly blue-shifted as shown in Fig. 6(a). This shift is mainly due to the bandgap-widening by the incorporation of Br^- or Cl^- [26]. The bandgap of the perovskite was estimated using a Tauc plot (Fig. 6b). The band gap of the sample without passivation, and Me_3SiCl, Me_3SiBr, Me_3SiI passivation was 1.40, 1.42, 1.41 and 1.40 eV, respectively. The variation trend in the band gap was also supported by the steady-state photoluminescence (PL) spectroscopy shown in Fig. 6(d). The PL peak was shifted from 885 nm (W/T) to 878 nm of Me_3SiCl passivation, 882 nm of Me_3SiBr, and 883 nm of Me_3SiI. In addition, the perovskite films passivated with Me_3SiX showed higher PL intensity than that without the passiva-

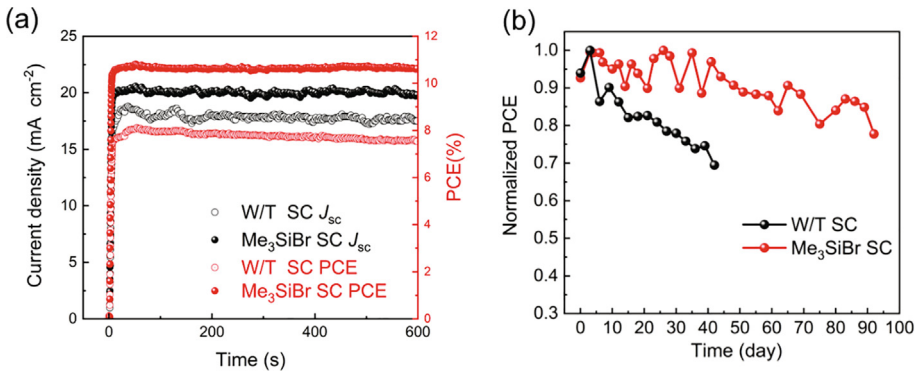

Fig. 2. (a) Steady-state PCE of Me_3SiBr with continuous AM 1.5 G one-sun illumination, and (b) PCE stability of W/T SC and Me_3SiBr SC.

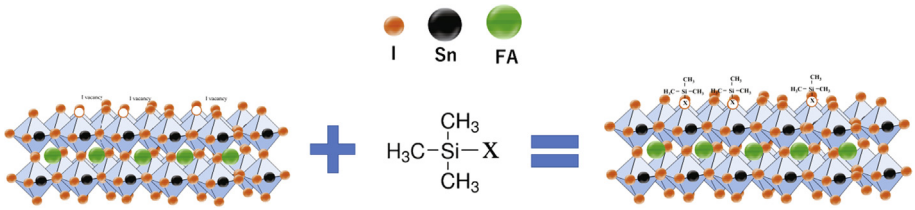

Fig. 3. One of the possible explanations of Me_3SiX surface passivation.

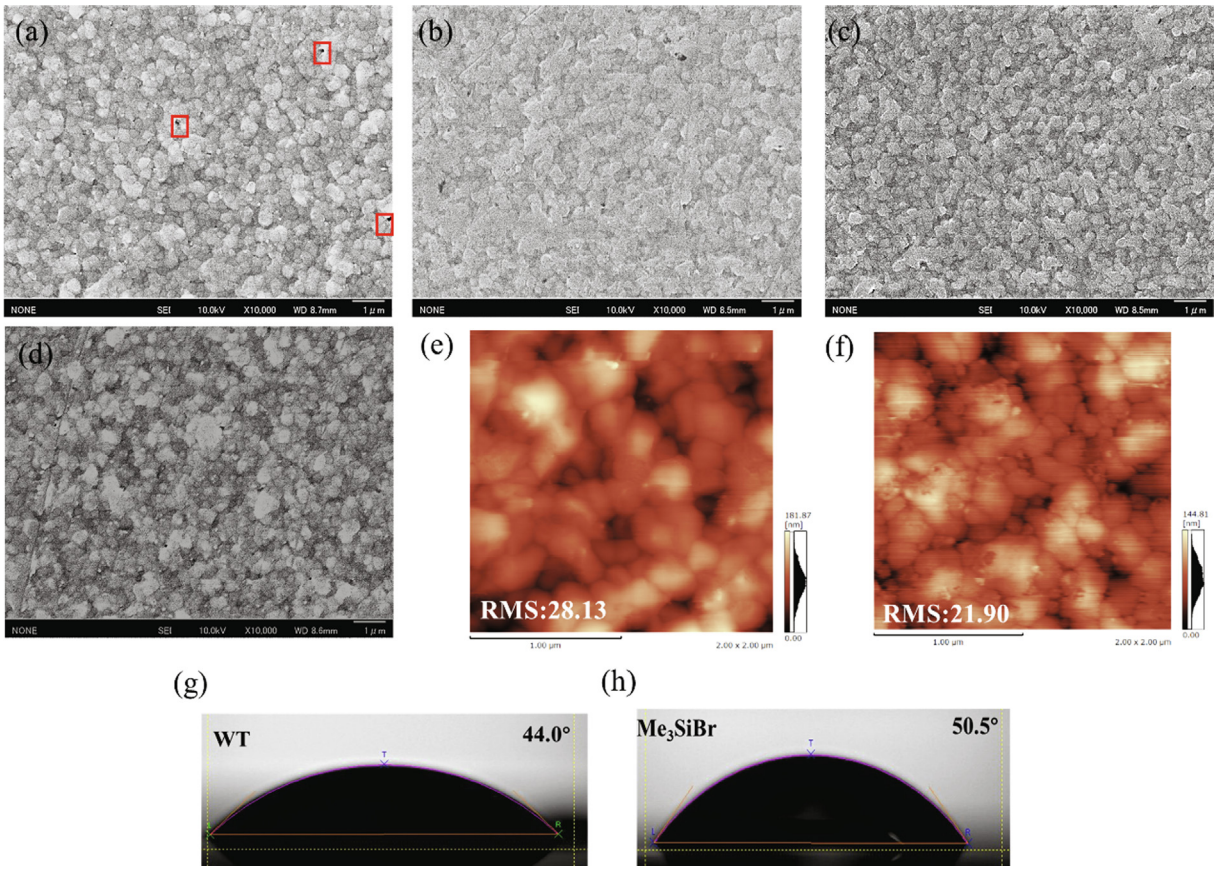

Fig. 4. SEM image of perovskite films of (a) without and with (b) Me_3SiBr, (c) Me_3SiCl and (d) Me_3SiI, and AFM image of (e) without passivation and (f) Me_3SiBr passivation, solid-water contact angles of (g) without passivation and (h) Me_3SiBr passivation.

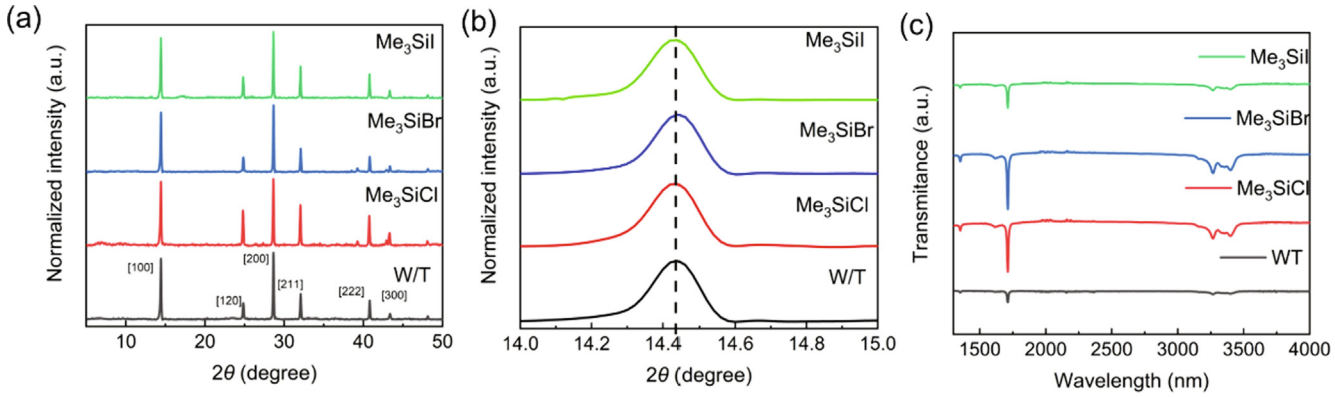

Fig. 5. (a) XRD patterns of $FA_{0.98}EDA_{0.01}SnI_3$ perovskite thin films with/without surface passivation. (b) Corresponding (100) peak at 2θ = 14.4°. (c) FTIR spectra (W/T transmittance scale expanded).

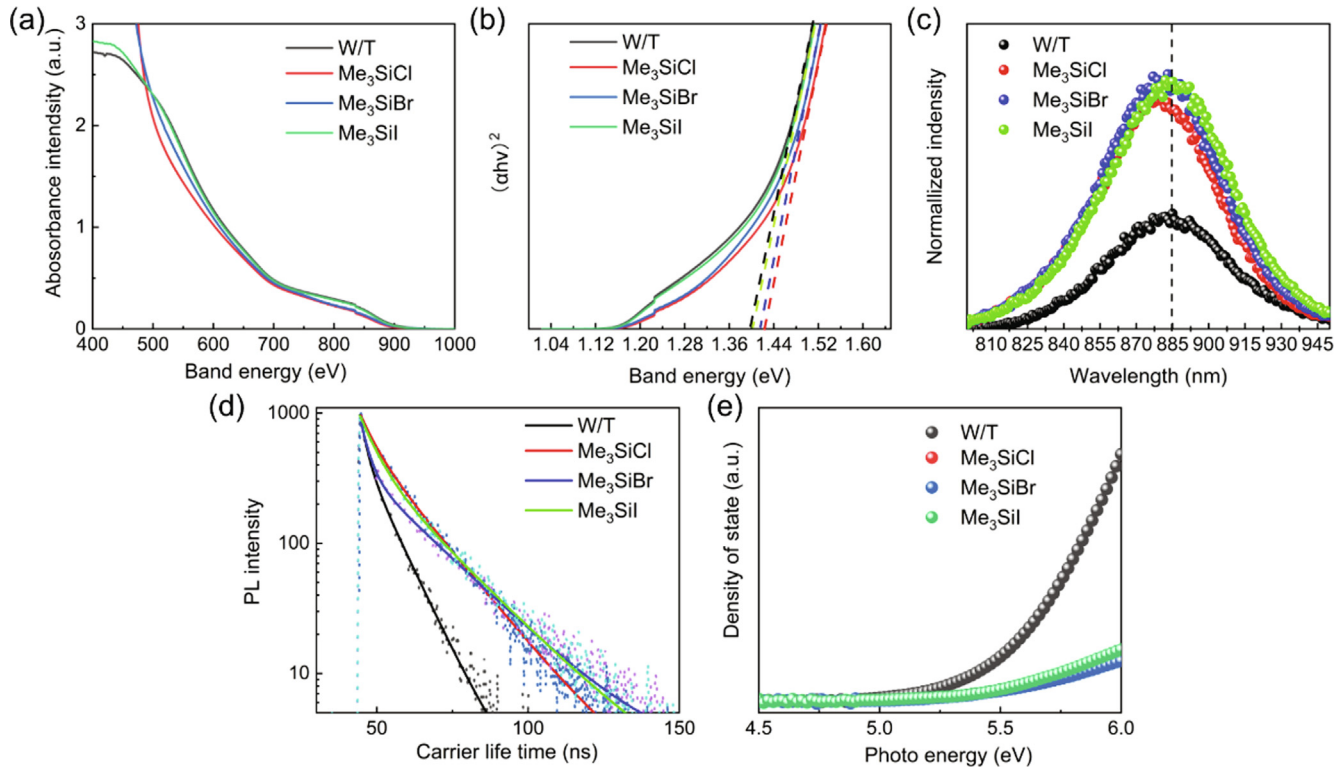

Fig. 6. (a) UV–Vis spectra and (b) calculated tauc plot, (c) PL spectra, (d) TRPL spectra of perovskite films (W/T transmittance scale expanded). (e) Density of states (DOS) as a function of photo energy for samples without and with Me_3SiBr, Me_3SiCl and Me_3SiI surface passivation.

tion, as demonstrated in Fig. 6(c). The higher PL intensity after the passivation is explained by the decreased trap density, because non-radiative trap assisted recombination is suppressed [52]. The blue shifted PL wavelength is also explained by the decrease in the shallow trap density. The concrete passivation structure by the silyl halide is not clear right now. Me_3Si^+ and halide ion may passivate the anion and cation defects sites, respectively [53].

As shown in Table S2, PL decay curves were fitted by the two components, namely, the fast component (τ_1) and slow decay component (τ_2). The fast decay component (τ_1) in the time resolved PL decay curve was extended from 2.11 nsec (W/T) to 4.52 nsec (Me_3SiCl), 5.45 nsec (Me_3SiBr), 3.72 nsec (Me_3SiI). Since the fast PL decay is assigned to the charge trapping process in the deep traps [54], the extended τ_1 after the surface passivation is explained by the lower deep trap density after the passivation. The lower density of states (DOS) in photoelectron yield spectroscopy (PYS) spectra (Fig. 6e, Fig. S9) after the surface passivation supports the explanation [55]. The τ_2 became longer in the following order, W/T (8.74 nsec) < Me_3SiI (11.72 nsec) < Me_3SiCl (15.33 nsec) < Me_3SiBr (18.90 nsec). The longer τ_2 after the passivation means that the band-to-band recombination emission was also extended, leading the conclusion that the shallow trap density was also decreased by the surface passivation. The average PL life time τ_{ave} were calculated using the follow equation.

$$\tau_{ave} = \frac{A_1\tau_1 + A_2\tau_2}{A_1 + A_2}$$

We calculated the average PL life time as 7.25 nsec (W/T), 13.74 nsec (Me_3SiCl), 15.08 nsec (Me_3SiBr),10.28 nsec (Me_3SiI). Based on others (XRD, FTIR, PL life time), it can be concluded that the Me_3SiBr showed better passivation effects than others. The boiling point for Me_3SiCl is 57 ℃, but the annealing temperature for perovskite was 70 ℃, which may cause uncontrolled volatilization. Me_3SiI was unstable and easy to decompose at room temperature. Therefore, it is recommended that the storage temperature was −20 ℃. The Me_3SiBr's boiling point was 79 ℃ and it was stable in the room temperature, resulting in better passivation effects.

Furthermore, the valence band energy (E_{VB}) levels were measured by PYS as shown in Fig. S9. From the band gap determined from the UV–Vis spectra and the E_{VB} from the PYS measurement, the energy band diagram was estimated as shown in the Fig. 7. After the passivation with Me_3SiX, the tin perovskite valence band energy became deeper in the following order: 5.12 eV (W/T) < 5.18 eV (Me_3SiCl) < 5.19 eV (Me_3SiBr) < 5.20 eV (Me_3SiBr). The surface Fermi level of the perovskite was shifted towards shallower value. Even after the passivation of the Sn perovskites by the silyl halide, the perovskite still showed p type character [56]. The result also supports the previous explanation that the p type defects, such

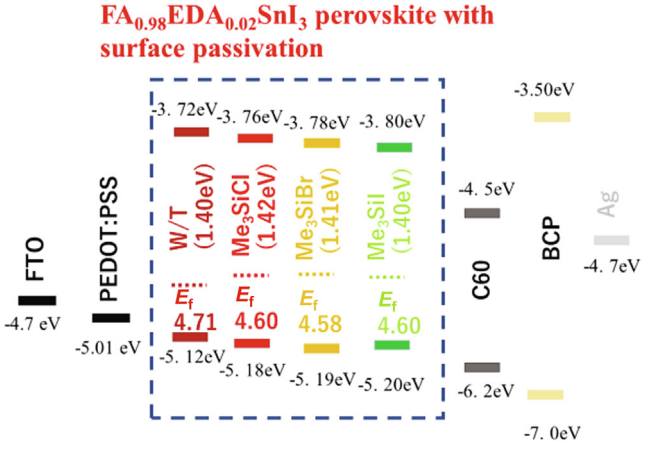

Fig. 7. Schematic diagram of energy band levels for inverted tin halide PKSCs.

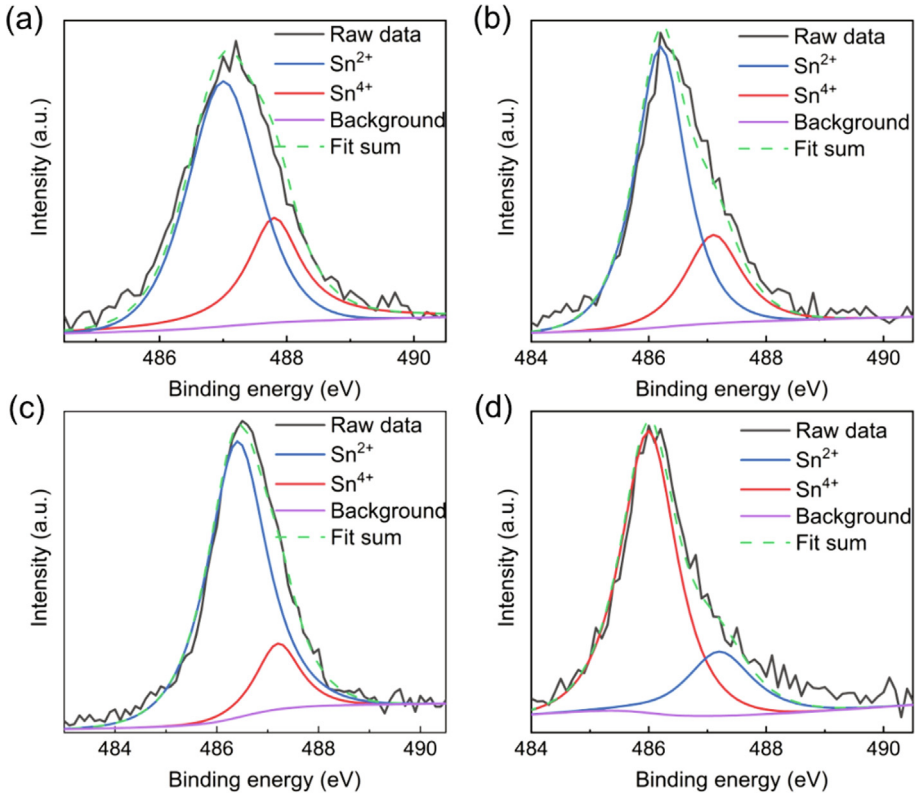

Fig. 8. XPS analysis of (a) the control film (W/T), (b) Me_3SiCl-passivated film (Me_3SiCl), (c) Me_3SiBr-passivated film (Me_3SiBr) and (d) Me_3SiI-passivated film (Me_3SiI).

as species of Sn^{4+} and the vacancy of Sn^{2+} are reduced by the passivation.

In order to analyze the cause of the improved photovoltaic performance, X-ray photoelectron spectroscopy (XPS) was measured. These results are summarized in the Fig. 8 and Table S3. These Sn 3d5/2 XPS peaks were fitted with Gaussian-Lorentz fit to distinguish the peaks of Sn^{2+} from Sn^{4+} [35]. The ratio of Sn^{4+}/ Sn^{2+} decreased from 0.45 (W/T) to 0.35 (Me_3SiCl), 0.18 (Me_3SiBr) and 0.27 (Me_3SiI). It is clear that the oxidation of Sn^{2+} is obviously retarded after the surface passivation [57]. Me_3SiBr passivation was most effective for decreasing Sn^{4+} species among them. This explained the enhanced stability and the best efficiency of Me_3SiBr passivation shown in Fig. 2(b)/Table 1. It has been reported that the oxygen molecules absorbed on the perovskite surface can easily turn to superoxide (O^{2-}) that triggers Sn-based perovskite oxidation and decomposition. In this work using Me_3SiX, we believe that Me_3Si^+ remains as the counter cation on the surface, which may form a hydrophobic protective layer to reduce the Sn^{2+} oxidization by small amount of oxygen or solvent such as DMSO (oxidant of Sn^{2+}), leading lower Sn^{4+}/ Sn^{2+} ratio [58]. As shown in the Table S3, the carrier density of the W/T sample (2.984×10^{16} cm^{-3}) estimated by hall effect measurement was higher than the other passivated samples, Me_3SiCl (1.165×10^{16} cm^{-3}), Me_3SiBr (2.933×10^{14} cm^{-3}) and Me_3SiI (1.712×10^{15} cm^{-3}) as shown in Table S3. These results also support the explanation on lower defect densities brought about by the silyl halide passivation [59].

4. Conclusions

We reported the passivation effect of the Sn perovskite solar cells with trimethylsilyl halide. All of the Me_3SiCl, Me_3SiBr and Me_3SiI were effective for the enhancement of the efficiency. These results were explained by longer PL decay, improved surface morphologies, lower defect densities after the surface passivation. Although all of these trimethylsilyl halide showed effective passivation effects, Me_3SiBr gave a little better result among them, which was well explained by the carrier densities in the perovskite layer. The stability was improved due to the hydrophobic protective layer after the surface passivation. The passivation will prevent the oxidation of Sn^{2+} to Sn^{4+}, and thereby increase the chemical stability of the perovskite film. Me_3SiBr SC showed the highest PCE of 12.22%, and 80% of the efficiency was maintained after 92 day-storage in nitrogen without encapsulation, while the W/T SC gave the PCE of 10.05% and the efficiency was decreased to 72% after the storage of 39 days. This work suggests the Me_3SiX surface passivation will be an important method to decrease the surface defects and increase the efficiency, as well to stabilize perovskite-based materials and devices.

Declaration of competing interest

The authors declare that they have no known competing financial interests or personal relationships that could have appeared to influence the work reported in this paper.

Appendix A. Supplementary data

Supplementary data to this article can be found online at https://doi.org/10.1016/j.jechem.2022.03.028.

References

[1] A. Kojima, K. Teshima, Y. Shirai, T. Miyasaka, J. Am. Chem. Soc. 131 (2009) 6050–6051.
[2] X. Gao, W. Luo, Y. Zhang, R. Hu, B. Zhang, A. Züttel, Y. Feng, M.K. Nazeeruddin, Adv. Mater. 32 (2020) 1905502.

[3] M.A. Kamarudin, D. Hirotani, Z. Wang, K. Hamada, K. Nishimura, Q. Shen, T. Toyoda, S. Iikubo, T. Minemoto, K. Yoshino, S. Hayase, J. Phys. Chem. Lett. 10 (2019) 5277–5283.
[4] X. Liu, M. Chen, Y. Zhang, J. Xia, J. Yin, M. Li, K.G. Brooks, R. Hu, X. Gao, Y.-H. Kim, Chem. Eng. J. (2021) 133713.
[5] S.F. Hoefler, G. Trimmel, T. Rath, Monatshefte Für Chemie-Chemical Mon. 148 (2017) 795–826.
[6] A. Toshniwal, V. Kheraj, Sol. Energy 149 (2017) 54–59.
[7] A. Abate, Joule 1 (2017) 659–664.
[8] F. De Angelis, ACS Energy Lett. 6 (2021) 1586–1587.
[9] W. Ke, M.G. Kanatzidis, Nat. Commun. 10 (2019) 1–4.
[10] E.-W.-G. Diau, E. Jokar, M. Rameez, ACS Energy Lett. 4 (2019) 1930–1937.
[11] Z. Zhang, A. Kumar Baranwal, S. Razey Sahamir, G. Kapil, Y. Sanehira, M. Chen, K. Nishimura, C. Ding, D. Liu, H. Li, Sol. RRL 5 (2021) 2100633.
[12] X. Jiang, H. Li, Q. Zhou, Q. Wei, M. Wei, L. Jiang, Z. Wang, Z. Peng, F. Wang, Z. Zang, J. Am. Chem. Soc. 143 (2021) 10970–10976.
[13] J. Zhou, M. Hao, Y. Zhang, X. Ma, J. Dong, F. Lu, J. Wang, N. Wang, Y. Zhou, Matter 5 (2022) 683–693.
[14] E. Aydin, M. De Bastiani, S. De Wolf, Adv. Mater. 31 (2019) 1900428.
[15] T.H. Chowdhury, R. Kaneko, T. Kaneko, K. Sodeyama, J.-J. Lee, A. Islam, Chem. Eng. J. (2021) 133745.
[16] T.A. Berhe, W.-N. Su, C.-H. Chen, C.-J. Pan, J.-H. Cheng, H.-M. Chen, M.-C. Tsai, L.-Y. Chen, A.A. Dubale, B.-J. Hwang, Energy Environ. Sci. 9 (2016) 323–356.
[17] S. Wang, Y. Jiang, E.J. Juarez-Perez, L.K. Ono, Y. Qi, Nat. Energy 2 (2016) 1–8.
[18] Q. Chen, H. Zhou, T.-B. Song, S. Luo, Z. Hong, H.-S. Duan, L. Dou, Y. Liu, Y. Yang, Nano Lett. 14 (2014) 4158–4163.
[19] D.-Y. Son, S.-G. Kim, J.-Y. Seo, S.-H. Lee, H. Shin, D. Lee, N.-G. Park, J. Am. Chem. Soc. 140 (2018) 1358–1364.
[20] M. Abdi-Jalebi, Z. Andaji-Garmaroudi, S. Cacovich, C. Stavrakas, B. Philippe, J.M. Richter, M. Alsari, E.P. Booker, E.M. Hutter, A.J. Pearson, Nature 555 (2018) 497–501.
[21] N. Li, S. Tao, Y. Chen, X. Niu, C.K. Onwudinanti, C. Hu, Z. Qiu, Z. Xu, G. Zheng, L. Wang, Nat. Energy 4 (2019) 408–415.
[22] P.N. Rudd, J. Huang, Trends Chem. 1 (2019) 394–409.
[23] M.I. Saidaminov, J. Kim, A. Jain, R. Quintero-Bermudez, H. Tan, G. Long, F. Tan, A. Johnston, Y. Zhao, O. Voznyy, Nat. Energy 3 (2018) 648–654.
[24] K. Nishimura, D. Hirotani, M.A. Kamarudin, Q. Shen, T. Toyoda, S. Iikubo, T. Minemoto, K. Yoshino, S. Hayase, A.C.S. Appl, Mater. Interfaces 11 (2019) 31105–31110.
[25] G. Kapil, T. Bessho, C.H. Ng, K. Hamada, M. Pandey, M.A. Kamarudin, D. Hirotani, T. Kinoshita, T. Minemoto, Q. Shen, T. Toyoda, T.N. Murakami, H. Segawa, S. Hayase, ACS Energy Lett. 4 (2019) 1991–1998.
[26] Z. Jin, B.-B. Yu, M. Liao, D. Liu, J. Xiu, Z. Zhang, E. Lifshitz, J. Tang, H. Song, Z. He, J. Energy Chem. 54 (2021) 414–421.
[27] W.-Q. Wu, P.N. Rudd, Z. Ni, C.H. Van Brackle, H. Wei, Q. Wang, B.R. Ecker, Y. Gao, J. Huang, J. Am. Chem. Soc. 142 (2020) 3989–3996.
[28] M. Yang, T. Zhang, P. Schulz, Z. Li, G. Li, D.H. Kim, N. Guo, J.J. Berry, K. Zhu, Y. Zhao, Nat. Commun. 7 (2016) 1–9.
[29] G. Giorgi, J.-I. Fujisawa, H. Segawa, K. Yamashita, J. Phys. Chem. C 119 (2015) 4694–4701.
[30] C. Wang, Y. Zhang, F. Gu, Z. Zhao, H. Li, H. Jiang, Z. Bian, Z. Liu, Matter 4 (2021) 709–721.
[31] E. Jokar, H.-S. Chuang, C.-H. Kuan, H.-P. Wu, C.-H. Hou, J.-J. Shyue, E. Wei-Guang Diau, J. Phys. Chem. Lett. 12 (2021) 10106–10111.
[32] A.K. Baranwal, S. Saini, Z. Wang, K. Hamada, D. Hirotani, K. Nishimura, M.A. Kamarudin, G. Kapil, T. Yabuki, S. Iikubo, Q. Shen, K. Miyazaki, S. Hayase, J. Electron. Mater. 49 (2020) 2698–2703.
[33] Q. Dong, Y. Fang, Y. Shao, P. Mulligan, J. Qiu, L. Cao, J. Huang, Science 347 (2015) 967–970.
[34] C. Li, Z. Song, D. Zhao, C. Xiao, B. Subedi, N. Shrestha, M.M. Junda, C. Wang, C. Jiang, M. Al-Jassim, Adv. Energy Mater. 9 (2019) 1803135.
[35] K. Nishimura, M.A. Kamarudin, D. Hirotani, K. Hamada, Q. Shen, S. Iikubo, T. Minemoto, K. Yoshino, S. Hayase, Nano Energy 74 (2020) 104858.
[36] T. Singh, T. Miyasaka, Adv. Energy Mater. 8 (2018) 1700677.
[37] C. Ding, F. Liu, Y. Zhang, S. Hayase, T. Masuda, R. Wang, Y. Zhou, Y. Yao, Z. Zou, Q. Shen, ACS Energy Lett. 5 (2020) 3224–3236.
[38] F. Yang, M.A. Kamarudin, G. Kapil, D. Hirotani, P. Zhang, C.H. Ng, T. Ma, S. Hayase, A.C.S. Appl, Mater. Interfaces 10 (2018) 24543–24548.
[39] Y. Guo, C. Liu, K. Inoue, K. Harano, H. Tanaka, E. Nakamura, J. Mater. Chem. A 2 (2014) 13827–13830.
[40] H. Li, G. Wu, W. Li, Y. Zhang, Z. Liu, D. Wang, S. Liu, Adv. Sci. 6 (2019) 1901241.
[41] Y. Jiang, E.J. Juarez-Perez, Q. Ge, S. Wang, M.R. Leyden, L.K. Ono, S.R. Raga, J. Hu, Y. Qi, Mater. Horizons 3 (2016) 548–555.
[42] H. Wang, C. Zhu, L. Liu, S. Ma, P. Liu, J. Wu, C. Shi, Q. Du, Y. Hao, S. Xiang, Adv. Mater. 31 (2019) 1904408.
[43] E. Jokar, C.-H. Chien, C.-M. Tsai, A. Fathi, E.-W.-G. Diau, Adv. Mater. 31 (2019) 1804835.
[44] A. Hosomi, H. Sakurai, Chem. Lett. 10 (1981) 85–88.
[45] R. Fessenden, J.S. Fessenden, Chem. Rev. 61 (1961) 361–388.
[46] X. Du, R. Qiu, T. Zou, X. Chen, H. Chen, H. Zhou, Adv. Mater. Interfaces 6 (2019) 1900413.
[47] W. Zeng, D. Cui, Z. Li, Y. Tang, X. Yu, Y. Li, Y. Deng, R. Ye, Q. Niu, R. Xia, Sol. Energy 194 (2019) 272–278.
[48] X. Wu, L. Zhang, Z. Xu, S. Olthof, X. Ren, Y. Liu, D. Yang, F. Gao, S.F. Liu, J. Mater. Chem. A 8 (2020) 8313–8322.
[49] J. Il Langford, A.J.C. Wilson, J. Appl. Crystallogr. 11 (1978) 102–113.
[50] M. Hu, R. Nie, H. Kim, J. Wu, S. Chen, B. Park, G. Kim, H.-W. Kwon, S. Il Seok, ACS Energy Lett. 6 (2021) 3555–3562.
[51] T.W. Jones, A. Osherov, M. Alsari, M. Sponseller, B.C. Duck, Y.-K. Jung, C. Settens, F. Niroui, R. Brenes, C.V. Stan, Energy Environ. Sci. 12 (2019) 596–606.
[52] K. Chen, P. Wu, W. Yang, R. Su, D. Luo, X. Yang, Y. Tu, R. Zhu, Q. Gong, Nano Energy 49 (2018) 411–418.
[53] W.S. Yang, B.-W. Park, E.H. Jung, N.J. Jeon, Y.C. Kim, D.U. Lee, S.S. Shin, J. Seo, E. K. Kim, J.H. Noh, Science 356 (2017) 1376–1379.
[54] T.P. Weiss, B. Bissig, T. Feurer, R. Carron, S. Buecheler, A.N. Tiwari, Sci. Rep. 9 (2019) 1–13.
[55] Z. Wang, A.K. Baranwal, P. Zhang, G. Kapil, T. Ma, S. Hayase, Nano Energy 66 (2019) 104180.
[56] N.K. Noel, S.D. Stranks, A. Abate, C. Wehrenfennig, S. Guarnera, A.-A. Haghighirad, A. Sadhanala, G.E. Eperon, S.K. Pathak, M.B. Johnston, Energy Environ. Sci. 7 (2014) 3061–3068.
[57] S.J. Yang, J. Choi, S. Song, C. Park, K. Cho, Sol. Energy Mater. Sol. Cells 227 (2021) 111072.
[58] N. Aristidou, C. Eames, I. Sanchez-Molina, X. Bu, J. Kosco, M.S. Islam, S.A. Haque, Nat. Commun. 8 (2017) 1–10.
[59] S. Teo, Z. Guo, Z. Xu, C. Zhang, Y. Kamata, S. Hayase, T. Ma, ChemSusChem 12 (2019) 518–526.